

Optimization of various isolation techniques to develop low noise, radiation hard double-sided silicon strip detectors for the CBM Silicon Tracking System

S. Chatterji^{a,*}, M. Singla^b, W.F.J. Müller^a, J.M. Heuser^a

^aGSI Helmholtzzentrum für Schwerionenforschung GmbH, Darmstadt, Germany

^bGoethe University, Frankfurt, Germany

Abstract

This paper reports on the design optimization done for Double Sided silicon microStrip Detectors (DSSDs) to reduce the Equivalent Noise Charge (ENC) and to maximize the breakdown voltage and Charge Collection Efficiency. Various isolation techniques have been explored and a detailed comparison has been studied to optimize the detector performance. For the evaluation of the performance of the silicon detectors, a radiation damage model has been included. The neutron fluence is expected to be $2 \times 10^{13} \text{ n}_{eq} \text{ cm}^{-2}$ per year for five years of expected CBM run with intermediate periods of warm maintenance, cold maintenance and shutdown. Transient simulations have been performed to estimate the charge collection performance of the irradiated detectors and simulations have been verified with experimental data.

Keywords: Double Sided silicon Strip Detector, Equivalent Noise Charge (ENC), radiation hardness, Transient simulation, Charge collection, Strip isolation, TCAD, SYNOPSIS

1. Introduction

The mission of the Compressed Baryonic Matter (CBM) [1] experiment at the Facility for Antiproton and Ion Research (FAIR) now under construction in Darmstadt, Germany, is to explore the QCD phase diagram in the region of high baryon densities. The layout of CBM detectors is driven by the corresponding experimental requirements concerning material budget, reaction rates, radiation tolerance, particle densities and selectivity. The detector will face the problem of measuring Au+Au interactions at 25 GeV/nucleon and up to 10MHz rate producing up to 1000 charged particle tracks per event. The core of the CBM detector is Silicon Tracking Station (STS) located in a large-aperture dipole magnet. The STS of the CBM will consist of eight tracking stations placed at a distance between 10-100 cm downstream of the target in a dipole magnet with internal field of 1 Tm. Each station is a modular structure of DSSDs of different sizes to match the non-uniform channel occupancy distribution from the beam pipe to the periphery. The sensors will be held by low-mass carbon fibre support structures with read-out electronics outside of the detector aperture, thus minimizing the Coulomb scattering of particles.

Table 1: Fluence profile of neutrons expected for CBM STS

Year	Fluence ($\text{n}_{eq} \text{ cm}^{-2}$)	$N_{eff} (\text{cm}^{-3})$	τ_e (ns)	τ_h (ns)	V_{fd} (V)	V_{op} (V)
1	2×10^{13}	2.80×10^{11}	1140	1050	28	70
2	4×10^{13}	-1.54×10^{11}	570	527	20	50
3	6×10^{13}	-5.35×10^{11}	380	351	44	110
4	8×10^{13}	-8.84×10^{11}	285	263	75	150
5	1×10^{14}	-12.1×10^{11}	228	211	100	200

*Corresponding author

Email address: S.Chatterji@gsi.de (S. Chatterji)

We aim to develop low-noise radiation hard DSSDs for the CBM STS. This is a challenging task keeping in mind that CBM uses fast self-triggering electronics; the shaping time of the front end chip used for early prototyping [2] is 19 ns (fast shaper) and 140 ns (slow shaper) respectively. The dominant contribution to the total Equivalent Noise Charge (ENC) is given by the series capacitive and the resistive components [3, 4, 5]. These two noise components are further inversely proportional to the shaping time of the preamplifier. The other less significant contributions to the total ENC like shot noise has also been taken into account in this study. Parameters relevant for the extraction of these two dominant components of ENC like interstrip capacitance and metal trace resistance has been studied. The various contributions to the total Equivalent Noise Charge (ENC) are given as follows:

(a) Series Capacitive Noise

$$a + b.C_{tot} \quad (1)$$

(b) Series Resistive Noise

$$24.C_{tot}(pF). \sqrt{R_s(\Omega)/\tau_s(ns)}e^- \quad (2)$$

(c)Shot Noise

$$108. \sqrt{I_{leak}(\mu A).\tau_s(ns)}e^- \quad (3)$$

(d)Parallel Resistive Noise

$$24. \sqrt{\tau_s(ns)/R_p(M\Omega)}e^- \quad (4)$$

where a and b are electrical parameters dependent on the front end electronics, C_{tot} is the total capacitance, R_s is the series resistance, τ_s is the shaping time of the preamplifier, I_{leak} is the leakage current and R_p corresponds to the bias resistor value.

Table 1 shows the expected neutron fluence for five years of expected CBM runtime. The maximum fluence is expected to be $1 \times 10^{14} \text{ n}_{eq}\text{cm}^{-2}$ which is similar to the Large Hadron Collider (LHC) radiation environment. One can observe a deterioration of carrier life time with fluence which will have an impact on the Charge Collection Efficiency (CCE), especially on the p-side since this side collects less mobile holes. In order to understand radiation damage, some of the CBM prototype DSSDs having dimension $1.6 \text{ cm} \times 1.6 \text{ cm}$ and resistivity $6 \text{ k}\Omega\text{cm}$ were irradiated at the KRI cyclotron facility in St. Petersburg, Russia. These detectors were measured just after irradiation without any periods of annealing. The variation of leakage current and interstrip resistance with neutron fluence has been measured. The radiation damage model implemented in TCAD simulations is able to reproduce the measured observations.

In order to investigate the life time of DSSDs, it is imperative to extract CCE as a function of fluence for which one has to understand strip isolation in particular on the ohmic side. Hence we are exploring various isolation techniques, for example P-stop, P-Spray, Modulated P-spray (conventional isolation techniques) and also a new isolation technique namely, Schottky barrier. TCAD simulations have been performed to optimize the total ENC, strip isolation and to maximize the breakdown voltage (V_{bd}) and CCE. Transient simulations can be used to extract the operating voltage of DSSDs which in turn depends on the isolation technique.

2. Structure of simulated devices

2.1. Simulated structure of DSSD

The AC-coupled DSSDs with n-type silicon substrate of $300 \mu\text{m}$ thickness have a strip width of $20 \mu\text{m}$, a pitch of $50 \mu\text{m}$ with orthogonal strips, as shown in Figure 1. The n-strips are orthogonal to the p-strips. We are using moderate resistivity n-type silicon of around $5\text{-}6 \text{ k}\Omega\text{cm}$ corresponding to effective doping concentration of $9 \times 10^{11} \text{ cm}^{-3}$ and $7.5 \times 10^{11} \text{ cm}^{-3}$, respectively. All p^+ and n^+ implants were approximated by assuming a Gaussian profile with a peak concentration of $5 \times 10^{19} \text{ cm}^{-3}$ at the surface. It is assumed that the lateral diffusion depth at the junction curvature of the implants is equal to 0.8 times the vertical junction depth (X_j). Depletion is attained by applying a positive voltage to the ohmic side and grounding the junction side. The thickness of the coupling oxide taken is around 200 nm while the interstrip gap is filled with a thicker oxide of around 800 nm . The surface oxide charge (Q_f) has been taken to be $3 \times 10^{11} \text{ cm}^{-2}$ before irradiation for a good quality oxide. For the $\langle 111 \rangle$ silicon orientation used in detector fabrication, the amount of charge is expected to increase and saturate at $3 \times 10^{12} \text{ cm}^{-2}$, under heavy irradiation of the

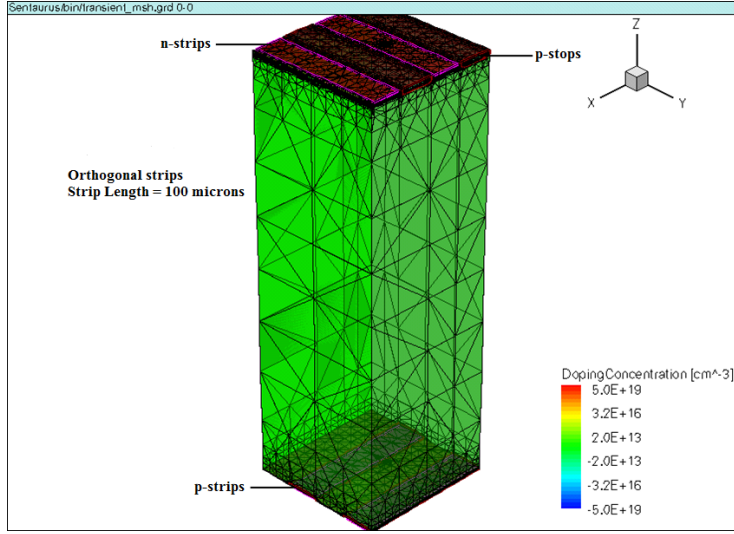


Figure 1: Slice of 3-dimensional DSSD grid having orthogonal strips.

63 order of a few hundred krad [6, 7]. The conventional isolation techniques namely P-stop, P-spray and Modulated P-
64 spray have been compared with a new isolation technique called Schottky barrier. The TCAD simulation grids having
65 these isolation techniques can be seen in Figure 2(a-d). The conventional isolation techniques have been defined by
66 assuming a Gaussian profile with a peak concentration of $5 \times 10^{19} \text{ cm}^{-3}$ at the surface for P-stop and $4 \times 10^{16} \text{ cm}^{-3}$ (low
67 dose) for P-spray. For modulated P-spray, an optimization study has been done for various combinations of P-stop
68 width and P-spray dose which will be discussed later in this paper. The new isolation technique namely Schottky
69 barrier can be defined either through metal work function value or through barrier height which in turn depends on the
70 substrate type and the metal used for schottky contact. For Aluminium, the barrier height is 0.72 eV for n-type silicon
71 while for p-type silicon, the barrier height is 0.58 eV [8, 9].
72 For accurate simulations, it is imperative to use correct boundary conditions. The reason being that we are simulating
73 only a part of a full device, hence we need to be sure that this does not affect the accuracy of the simulation. One
74 possible way to do this is to simulate larger area of the device and then to look at the results only in the central region,
75 away from the boundaries. The other approach is to simulate some repeating unit of device and then to make sure that
76 the boundary conditions are appropriate. The default is to use reflecting (Neumann) boundary conditions for a device
77 with transitional symmetry and mirror symmetry. However in our device with orthogonal strips, there is transitional
78 symmetry in x and y direction but no mirror symmetry. Hence we have applied periodic boundary conditions (PBC)
79 in x and y direction for device having orthogonal strips.

80 2.2. Models implemented in TCAD simulation

81 SYNOPSIS [10], a finite element semiconductor simulation package was used to determine the electrical be-
82 haviour of these devices. The effective doping concentration (N_{eff}) is parameterized using Hamburg model [11, 12]
83 which consist of three components, a short term beneficial annealing component, a stable damage part and a re-
84 verse annealing component. To incorporate the effect of increase in leakage current with fluence, the minority carrier
85 lifetime τ has been changed in our simulation package using the definition of Kraner [13] as follows:

$$1/\tau = 1/\tau_0 + \beta \cdot \phi_{eq} \quad (5)$$

86 where τ_0 is the minority carrier lifetime of the initial wafer, ϕ_{eq} is the integrated fluence, and β is the trapping time.
87 The default value of τ_0 for the electrons and holes is $10 \mu\text{s}$ and $3 \mu\text{s}$ in Sentaurus Device. These values have been
88 modified in Scharfetter relation [14] to a value of 1 ms for electrons and 0.3 ms for holes as is expected for detector
89 grade silicon.

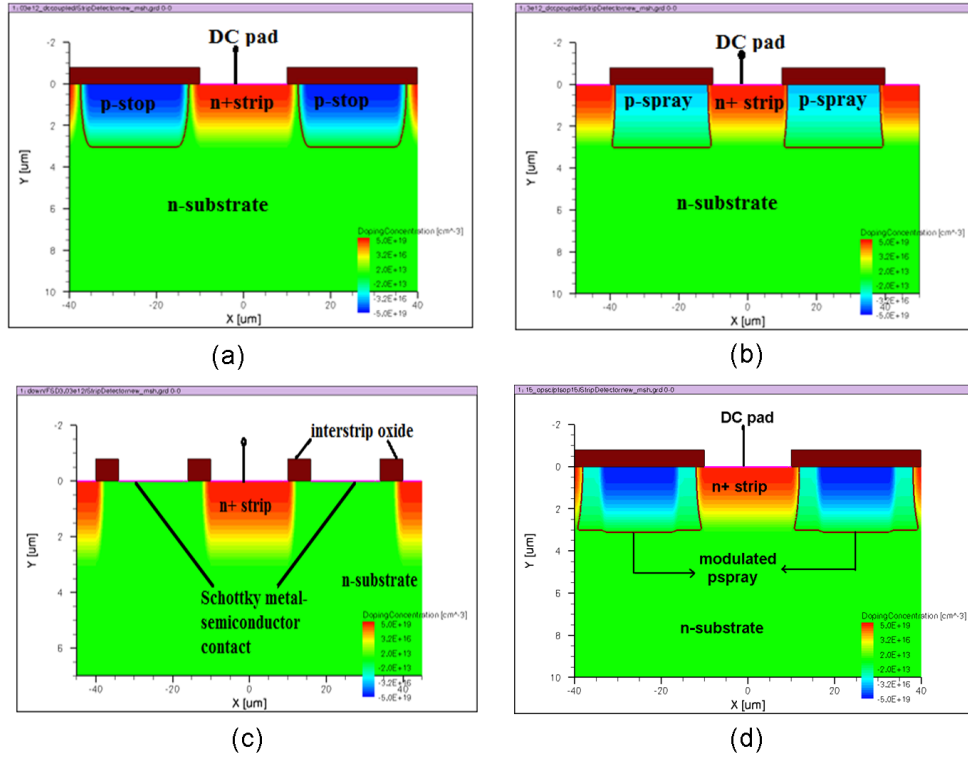


Figure 2: Simulated TCAD grid of DSSD having four different isolation techniques (a) P-stop; (b) P-spray; (c) Schottky barrier; (d) Modulated P-spray.

90 When high-energy particles such as hadrons pass through a detector, they collide with silicon atoms and displace
 91 them from their lattice sites, resulting in pairs of interstitial atoms and vacancies. These defects may recombine,
 92 or they may form complexes with each other or with existing impurities in the silicon [15, 16, 17]. These defects
 93 introduce extra energy levels within the bandgap of the silicon. SYNOPSIS simulates this bulk radiation damage by
 94 directly modelling the dynamics of these traps [18]. So, the user has to provide SYNOPSIS with the concentrations
 95 and parameters of the traps. The trap model used here is based on the work done at the University of Perugia [19].

Table 2: Comparison of measured and simulated data for irradiated DSSDs

Fluence $n_{eq} \text{ cm}^{-2}$	Leakage Current @ 20°C (nA)		V_{fd} (V)	
	Measured	Simulated	Measured	Simulated
2.06×10^{12}	5.4×10^3	5.68×10^3	47 ± 5	45
3.03×10^{12}	9.5×10^3	8.31×10^3	29 ± 5	37
3.93×10^{12}	10.7×10^3	10.7×10^3	29 ± 5	32
11.20×10^{12}	35.1×10^3	30.3×10^3	9 ± 5	9
20.60×10^{12}	66.5×10^3	58.8×10^3	50 ± 5	48

96 3. Results and discussion

97 3.1. Leakage current and depletion behaviour of sensors

98 Current-Voltage (I-V) characteristics were simulated for DSSDs and compared with measurements. In DSSDs,
 99 most of the bulk leakage current is due to electron-hole pairs being produced by Shockley-Read-Hall (SRH) gener-

Table 3: Expected power consumption of irradiated DSSDs

Fluence $n_{eq} \text{ cm}^{-2}$	V_{op} (V)		Leakage Current @ -10^0C (nA)	$R_{int} @ V_{op}$ (G Ω)		Power Consumption $V_{op} \times I_{leak}$ ($\mu\text{W mm}^{-1}$)
	Measured	Simulated		Measured	Simulated	
3.03×10^{12}	60 ± 5	55	346	0.2 ± 0.05	1	8.10×10^{-2}
3.93×10^{12}	64 ± 5	62	448	0.1 ± 0.05	1.5	11.20×10^{-2}
11.20×10^{12}	8 ± 2	20	1250	0.1 ± 0.05	0.6	3.90×10^{-2}
20.60×10^{12}	120 ± 10	105	2420	0.1 ± 0.05	0.2	113.44×10^{-2}

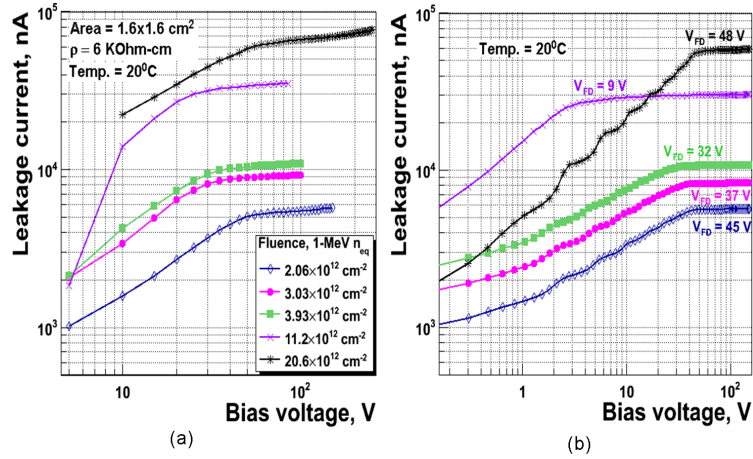


Figure 3: Current-Voltage characteristics of irradiated DSSDs having P-stop isolation obtained through (a) measurements and (b) simulations.

100 ation [18] in the depletion region, which are then swept to the electrodes by the electric field. Some of the CBM
 101 prototype DSSDs have been irradiated with neutrons at KRI cyclotron facility in St. Petersburg, Russia. The irradiated
 102 data are shown in Figure 3(a). The full depletion voltage (V_{fd}) indicates that the type inversion occurs at around
 103 $11.20 \times 10^{12} n_{eq} \text{ cm}^{-2}$. The full depletion voltage decreases with increasing fluence until the point of type inversion
 104 and after type inversion it starts increasing with fluence. The simulated I-V curve shown in Figure 3(b) matches
 105 qualitatively with the measured curves for the irradiated sensors. A comparison of measured parameters with the
 106 simulated values is shown in Table 2. The leakage current increases with fluence, thus increasing the shot noise com-
 107 ponent in the ENC calculations. However this can be controlled by operating the sensors at cryogenic temperatures.
 108 The extracted damage constant (α) from simulation is about $3.73 \times 10^{-17} \text{ A cm}^{-1}$ while from measurement is about
 109 $4.2 \times 10^{-17} \text{ A cm}^{-1}$. A similar agreement has also been found for DSSDs having Schottky barrier both for unirradiated
 110 and for the irradiated ones including the effect of annealing as can be seen in the figures 4(a) and 4(b).

111 3.2. Series Capacitance and resistance of sensors

112 Series capacitance and series resistance (trace resistance) are the dominant factors contributing to the total ENC.
 113 The strip capacitance is the sum of the capacitance to the backplane and direct capacitance to the adjacent strips
 114 (interstrip capacitance). For small pitch microstrip detectors having $300 \mu\text{m}$ thickness, the interstrip capacitance (C_{int})
 115 is expected to dominate over the backplane capacitance. We have used TCAD simulations to extract the C_{int} both
 116 before and after irradiation. Figure 5 shows the measured variation of ohmic side C_{int} versus bias voltage (V_{bias}) for
 117 non-irradiated DSSDs having P-spray isolation. Figure 6 shows the simulated variation of C_{int} versus V_{bias} for both
 118 P-stop and P-spray isolation. For both the cases, it has been found that C_{int} initially increases till the point of full
 119 depletion. After full depletion, there is a steep fall in C_{int} and then it saturates.

120 One can notice that there is a nice match between simulated and measured C_{int} especially after full depletion. Also
 121 it becomes clear that P-stop isolation gives lower capacitance as compared with P-spray isolation. We have simulated
 122 the expected variation of C_{int} versus V_{bias} for Schottky barrier isolation in order to compare it with the conventional

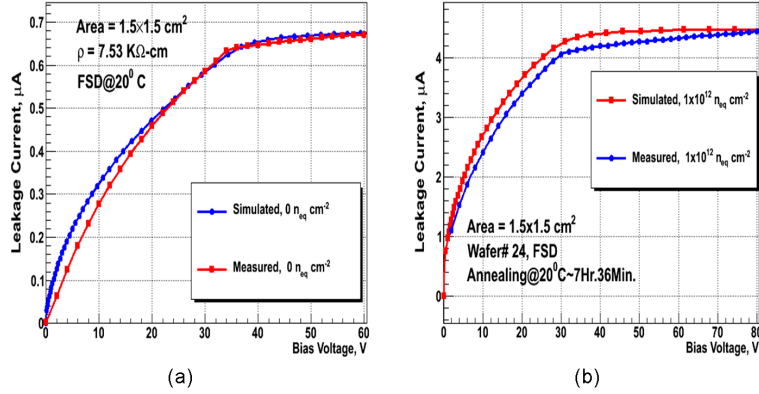


Figure 4: Comparison of measured variation of leakage current vs. bias voltage with simulation for DSSDs having schottky barrier isolation (a) at Zero fluence and (b) after irradiation with $1 \times 10^{12} \text{ n}_{eq} \text{ cm}^{-2}$.

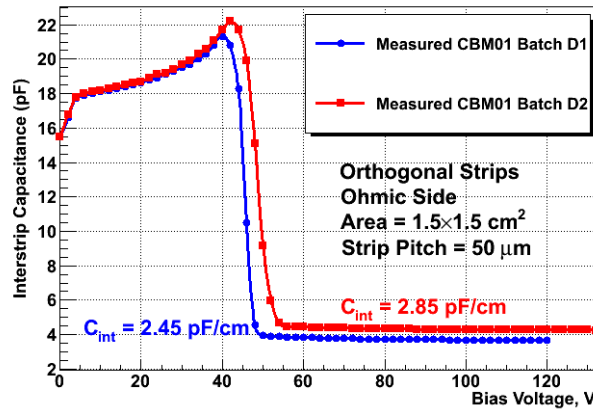


Figure 5: Measured variation of C_{int} with bias voltage for DSSDs having P-spray isolation.

123 isolation techniques. It is clear from Figure 7 that C_{int} for Schottky barrier isolation is slightly lower as compared with
 124 P-stop isolation technique after full depletion. However before full depletion, C_{int} for Schottky barrier isolation is too
 125 high both for unirradiated as also for irradiated DSSDs which could be detrimental if the DSSDs have to be operated
 126 under-depleted at high fluences. We wanted to study if there is an impact of irradiation on the interstrip capacitance.
 127 For this purpose, we have used our radiation damage model which has already been validated with measurements.
 128 Figure 8 shows the simulated variation of ohmic side C_{int} versus V_{bias} after irradiation for DSSDs equipped with
 129 P-stop. The shape of the C_{int} remains the same as for non-irradiated case. We do not observe a drastic change in
 130 the value of C_{int} with irradiation. It can be noted that the value of C_{int} before full depletion initially decreases with
 131 fluence till the point of type-inversion and increase thereafter. Figure 9 shows the variation of metal trace resistance as
 132 a function of frequency. The measured resistance has been found to be around $21 \Omega \text{ cm}^{-1}$. The contribution from the
 133 parallel resistance to the ENC is negligible since it is inversely proportional to the value of bias resistor whose value
 134 is of order of few $\text{M} \Omega$'s.

135 3.3. Strip isolation and the charge collection efficiency

136 In order to investigate the life time of DSSDs, it is imperative to extract CCE as a function of fluence. One
 137 can understand strip isolation by studying interstrip resistance (R_{int}) in particular on the ohmic side. In figure 10(a),

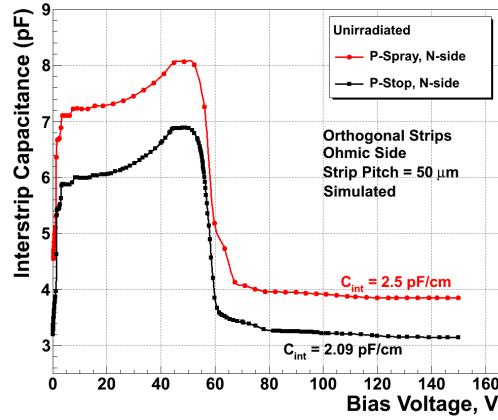


Figure 6: Simulated variation of C_{int} with bias voltage for DSSDs having P-spray and P-stop isolation.

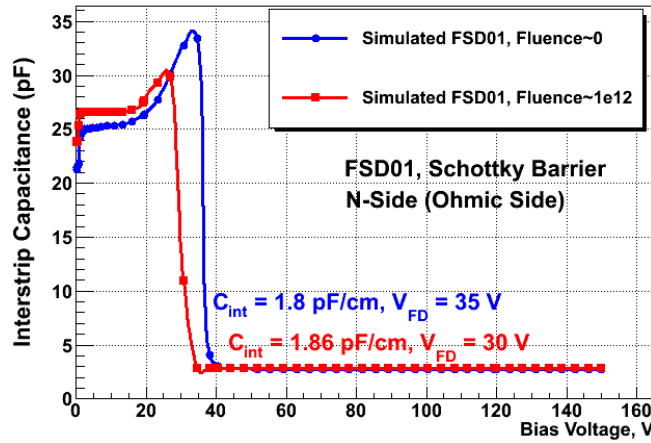


Figure 7: Simulated variation of C_{int} with bias voltage for DSSDs having Schottky barrier isolation.

138 the measured variation of ohmic side R_{int} with V_{bias} can be seen for different fluences. For the fluences up to type
 139 inversion, interstrip resistance is very low before full depletion and it increases steeply at full depletion and continues
 140 to increase slightly thereafter. However for type-inverted sensors, interstrip resistance is of the order of tens of $M\Omega$'s
 141 even before full depletion and saturates at around $100 M\Omega$ after the operating voltage is reached. In type inverted
 142 sensors, this effect can be attributed to electron accumulation layer [20] due to which the type of silicon between
 143 the p-strips remains n-type as can be seen in Figure 11. To confirm this effect, e^- density between the p-strips has
 144 been extracted as shown in Figure 12. The high e^- density between p-strips confirm the presence of n-type substrate
 145 between the p-strips even after type-inversion. Thus, isolation on the p side is realized even at low biases after type
 146 inversion. Figure 10(b) shows the simulated values of interstrip resistance for the irradiated sensors for the same
 147 fluences as in measurements. A good match has been found for the fluences up to type inversion. However there is
 148 some discrepancy with the type inverted case for biases below full depletion. The simulated trap model is not able
 149 to reproduce the effect of electron accumulation layer in R_{int} simulation. Though this effect is reflected accurately
 150 in the transient simulations as discussed below. Also it should be noted from Figure 10(b) that the operating voltage
 151 is around 1.5-2.0 times the V_{fd} depending on the fluence. It is advisable to reduce the operating voltage since it
 152 directly increases the power consumption. Table 3 shows the expected power consumption of DSSDs irradiated up to

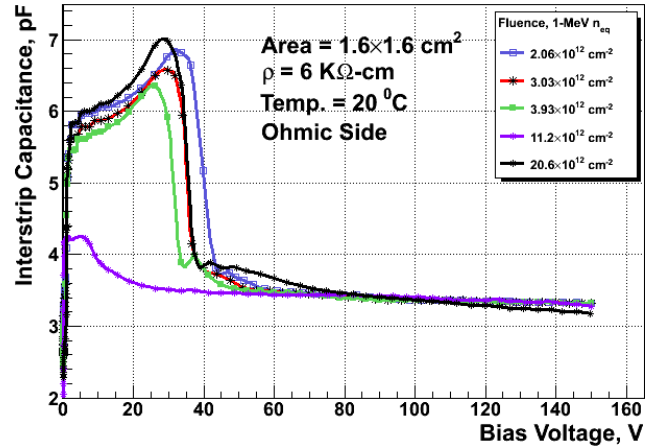


Figure 8: Interstrip capacitance vs. bias voltage for irradiated DSSDs equipped with P-stop isolation technique.

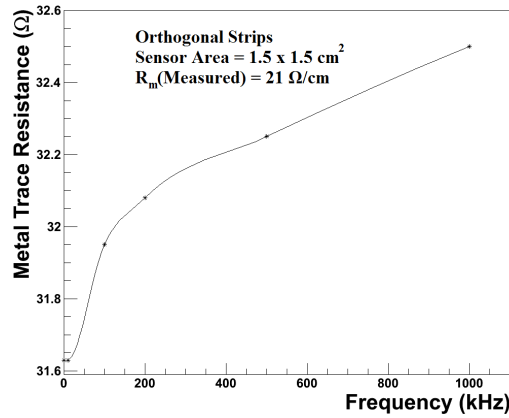


Figure 9: Measured trace resistance vs. frequency for DSSD equipped with P-spray isolation technique.

153 $2.06 \times 10^{13} \text{ n}_{eq} \text{ cm}^{-2}$. One can observe that the power consumption increases steeply after type-inversion.

154 We have studied the charge collection through transient simulations by shooting a Minimum Ionizing parti-
 155 cle (MIP) orthogonally on one of the junction side strips and observing the charge collection on the corresponding
 156 ohmic side strip. Figures 13(a) and 13(b) show the transient signals observed on the p-side of DSSD exposed to a
 157 fluence of $3.93 \times 10^{12} \text{ n}_{eq} \text{ cm}^{-2}$ and $20.60 \times 10^{12} \text{ n}_{eq} \text{ cm}^{-2}$ respectively. One can infer from these plots that the charge
 158 collection time in either case can be improved by operating the sensors at high bias voltage since in either case less mo-
 159 bile holes are being collected which can be confirmed from the polarity of the signal. Figure 14(a) and 14(b) show the
 160 transient signals observed on the n-side of DSSD exposed to a fluence of $3.93 \times 10^{12} \text{ n}_{eq} \text{ cm}^{-2}$ and $20.60 \times 10^{12} \text{ n}_{eq} \text{ cm}^{-2}$
 161 respectively. It can be noted that for this case, charge collection is much faster as n-side is collecting electrons. These
 162 transient signals have been integrated over time to extract the collected charge.

163 In order to validate the transient simulations, we have reproduced the experimentally observed CCE for thin ($140 \mu\text{m}$)
 164 and thick ($300 \mu\text{m}$) n-in-p detectors irradiated to a fluence of $5.0 \times 10^{14} \text{ n}_{eq} \text{ cm}^{-2}$. The structure and substrate doping of
 165 the simulated device matched with those tested in Ref. [21]. The comparison of the simulated CCE with the measure-
 166 ments can be seen in Figure 15. The simulation results agree with measurements within 10 % error thus validating the
 167 transient simulations.

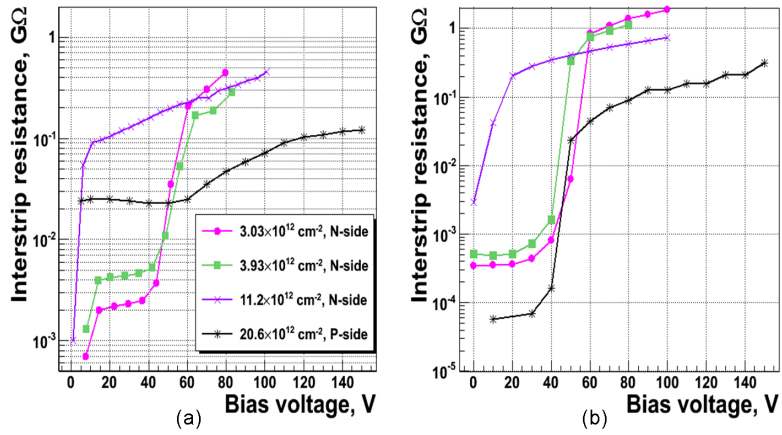


Figure 10: Variation of interstrip resistance vs. bias voltage of irradiated DSSDs having P-stop isolation technique obtained through (a) measurements and (b) simulations.

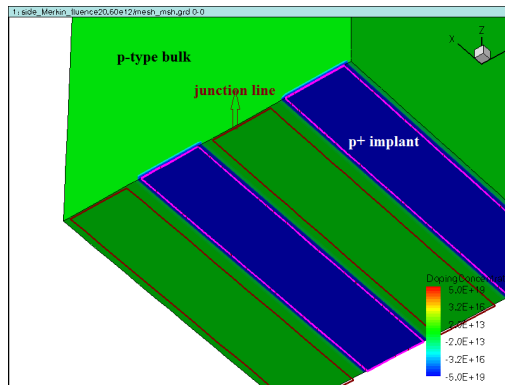


Figure 11: Junction line formed by type-inverted bulk and e^- accumulation layer on the ohmic side.

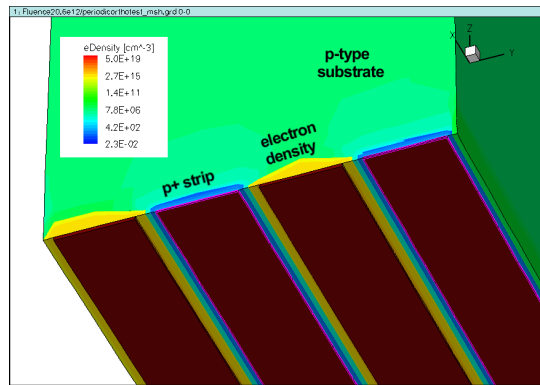


Figure 12: Electron density between the P-strips in type-inverted DSSD.

168 Figure 16 shows the variation of collected charge versus V_{bias} for the same fluences as used for irradiation. The

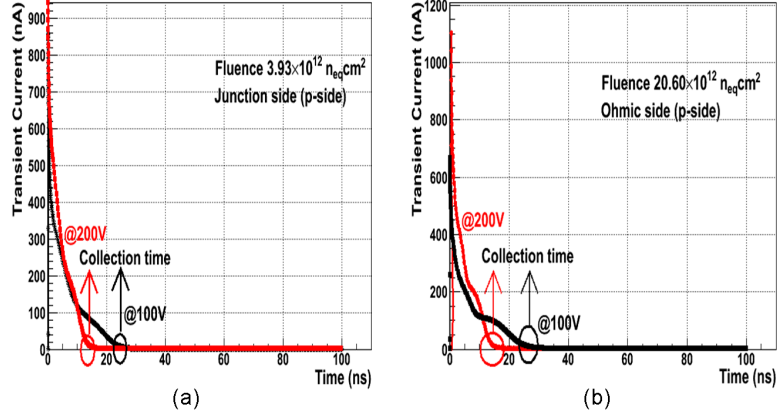


Figure 13: Transient signal on the p-side at V_{bias} 100V & 200V for DSSDs irradiated to (a) $3.93 \times 10^{12} \text{ n}_{eq} \text{ cm}^{-2}$ and (b) $20.60 \times 10^{12} \text{ n}_{eq} \text{ cm}^{-2}$.

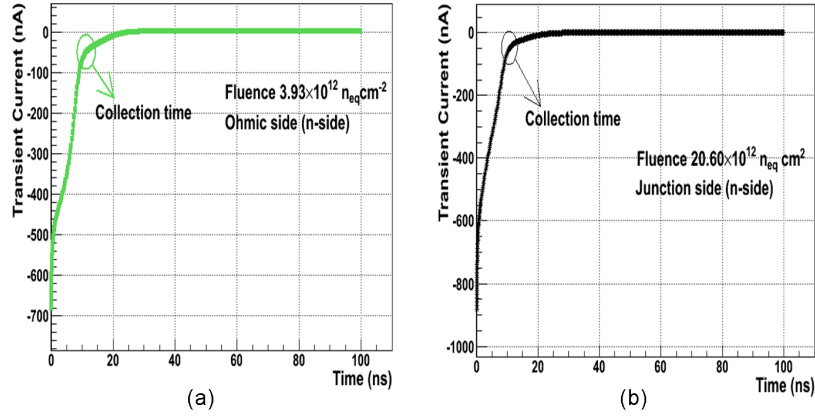


Figure 14: Transient signal on the n-side at V_{bias} 100V for DSSD irradiated to (a) $3.93 \times 10^{12} \text{ n}_{eq} \text{ cm}^{-2}$ and (b) $20.60 \times 10^{12} \text{ n}_{eq} \text{ cm}^{-2}$.

169 charge collection follows the same variation as measured R_{int} does with V_{bias} . Figure 17 shows the charge pickup
 170 (crosstalk) by neighbouring strip on the ohmic side as a function of V_{bias} . As expected, the crosstalk initially increases
 171 with V_{bias} for all the fluences since the depletion region gets wider, and so the amount of charge sharing between the
 172 neighbouring strips will increase. On the other hand, increasing the bias will also improve the drift velocity, which
 173 tends to reduce charge sharing. So, as the detector nears full depletion, this second effect becomes more important,
 174 and the crosstalk slowly decreases. It becomes clear from Figures 16 and 17 that the main impact of irradiation is the
 175 deterioration of CCE. We have tried to extract a mathematical model for the dependence of CCE on the carrier life
 176 time as can be seen in Figure 18.

177 3.4. Design optimization of isolation techniques in DSSDs

178 Table 4 shows the expected breakdown voltage (V_{bd}) for DSSDs exposed to a low fluence (before type-inversion)
 179 and high fluence (after type-inversion) having three isolation techniques namely P-stop, P-spray and Schottky barrier.
 180 The CBM plans to use floating electronics [22], hence for V_{bd} simulations, DC coupled DSSDs have been considered.
 181 One can notice that in all the three cases, the V_{bd} deteriorates with fluence. For DSSDs having conventional isolation

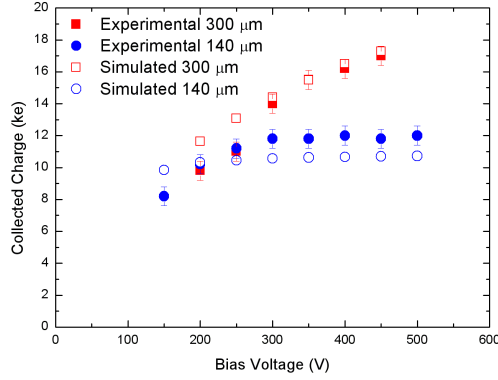


Figure 15: Comparison of measured CCE for thin and thick n-in-p detectors with transient simulations.

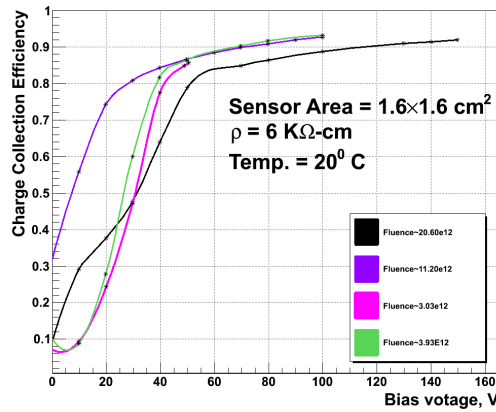


Figure 16: CCE versus bias voltage for irradiated DSSDs equipped with P-stop isolation.

182 techniques, this happens since before type-inversion the electric field is distributed on either sides while after type-
 183 inversion the high electric field exists only on the n- side. This can be seen from the Figure 19 . However in the case
 184 of DSSDs having Schottky barrier, the critical electric field responsible for breakdown occurs in the oxide between
 185 n-strips and schottky contact as can be seen from Figure 20. Hence the V_{bd} deteriorates with fluence since there is an
 186 increase in surface oxide charge with fluence. One can infer from Table 4 that in terms of breakdown performance,
 187 the Schottky barrier is the best choice.

188 Interstrip capacitance (C_{int}) has been simulated for DSSDs having conventional isolation techniques and also for
 189 DSSDs equipped with Schottky barrier both for low and high fluences as can be seen from Table 4. One can notice
 190 that the C_{int} on the p-side is lower as compared with n-side for DSSDs equipped with P-stop and P-spray. This again
 191 can be explained based on e^- accumulation layer [20] which helps in coupling the n-strips while doing an opposite
 192 effect between the p-strips. Also one can notice that with increasing fluence, the C_{int} on the p-side increases in larger
 193 proportion as compared with n-side. This could be explained since the silicon bulk inverts to P-type at higher fluence,
 194 which helps to overcome the inhibition of hole density by the electron accumulation layer between the p-strips. In the
 195 case of DSSDs having schottky barrier, a steep rise in the value of C_{int} is observed after type-inversion on the p-side.
 196 This has also been observed during measurements. Since the C_{int} on the p-side of DSSDs having schottky barrier is

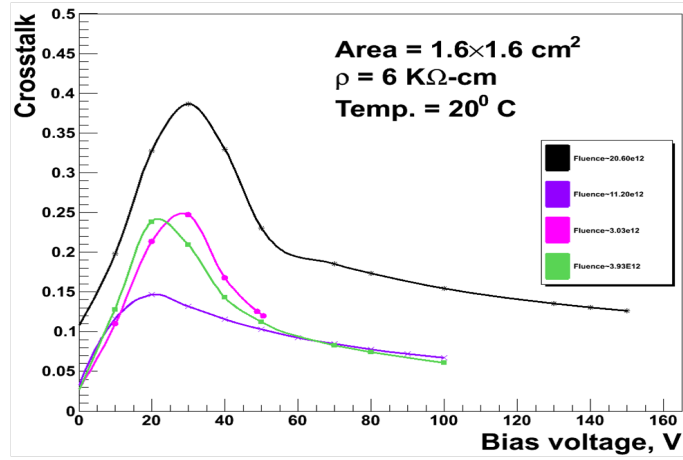


Figure 17: Cross-talk versus bias voltage for irradiated DSSDs equipped with P-stop isolation.

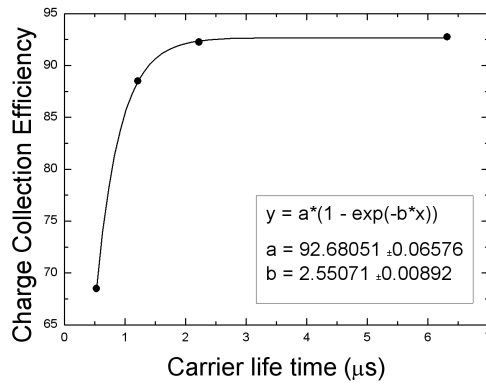


Figure 18: Modelling of dependence of CCE on carrier life time.

Table 4: Comparison of conventional isolation techniques with schottky barrier isolation in terms of static and dynamic parameters.

Isolation Technique	Fluence ($n_{eq} \text{ cm}^{-2}$)	V_{bd} (V)	C_{int} (pF cm^{-1})		R_{int} @ 80V (M Ω)	CCE @ 80V (%)
			n-side	p-side		
P-spray	3.93×10^{12}	524	2.6	1.7	1250	93
	20.60×10^{12}	450	2.7	2.1	104	86.25
P-stop	3.93×10^{12}	860	2.1	1.7	1136	91.25
	20.60×10^{12}	750	2.29	2.1	125	86.25
Schottky Barrier	3.93×10^{12}	1450	2.05	1.7	19.64	79
	20.60×10^{12}	1350	1.8	4.0	8	77.5

197 too high at high fluence, this is not a good choice for isolation technique in terms of capacitive noise.

198 Figure 21 shows the variation of R_{int} versus V_{bias} for DSSDs equipped with P-stop, P-spray and Schottky barrier
 199 at low and high fluences. One can observe that for low fluence, P-spray gives better isolation as compared with P-stop.
 200 The operating voltage with P-spray isolation technique is reached at 35 V while with P-stop, the operating voltage

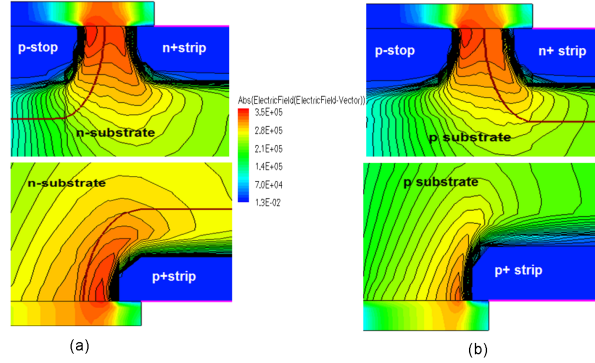


Figure 19: Simulated electric field distribution on n and p side of the DSSD at breakdown irradiated to a fluence of (a) $3.93 \times 10^{12} \text{ n}_{eq} \text{ cm}^{-2}$ (before type-inversion) and (b) $20.60 \times 10^{12} \text{ n}_{eq} \text{ cm}^{-2}$ (beyond type-inversion).

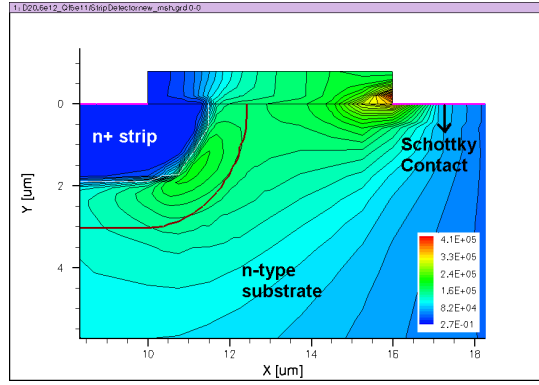


Figure 20: Simulated electric field distribution at breakdown for DSSD equipped with schottky barrier.

Table 5: Optimization of modulated p-spray

p-spray dose (cm^{-3})	1×10^{15} (very low dose)		4×10^{16} (low dose)		8×10^{16} (medium dose)		12×10^{16} (high dose)					
	V_{bd} (V)	C_{int} (pF cm^{-1})		V_{bd} (V)	C_{int} (pF cm^{-1})		V_{bd} (V)	C_{int} (pF cm^{-1})				
		n-side	p-side		n-side	p-side		n-side	p-side			
5	1125	1.56	1.75	490	2.405	1.75	210	2.46	1.76	161	2.47	1.77
10	1125	1.5	1.75	480	2.4	1.75	205	2.46	1.76	160	2.47	1.77
15	1150	1.6	1.75	488	2.37	1.75	205	2.43	1.76	160	2.47	1.77
20	650	2.09	1.75	450	2.51	1.75	205	2.42	1.76	160	2.47	1.77

201 is at 45 V. The R_{int} for DSSD with schottky barrier is comparatively very low and its operating voltage is reached at
 202 90 V. For high fluence, the R_{int} of P-spray and P-stop are almost same and both reach their operating voltage at around
 203 70V. Again for DSSD having schottky barrier, R_{int} is throughout low and the operating voltage is reached at 100 V.
 204 As discussed in Section 3.3, higher operating voltage means higher power consumption which could lead to thermal
 205 runaway at high fluences. Figure 22 shows the variation of CCE versus V_{bias} for DSSDs having conventional isolation
 206 techniques and schottky barrier. Again the CCE mimics the variation of R_{int} with V_{bias} . For low fluence, P-spray gives
 207 better CCE as compared with P-stop while Schottky barrier gives the worst performance in terms of CCE. As in the
 208 case of R_{int} , at high fluence, the CCE of P-stop and P-spray is same while for schottky barrier, the CCE is very poor.
 209 Hence in terms of power consumption and CCE, it seems not optimal to use Schottky barrier as an effective isolation

Table 6: Comparison between p-stop, p-spray and optimized modulated p-spray at low and high fluence.

Isolation Technique	Fluence ($n_{eq} \text{ cm}^{-2}$)	V_{bd} (V)	C_{int} (pF cm^{-1})	CCE %
P-stop	2×10^{13}	800	2.08	93.15
	1×10^{14}	610	2.09	88.87
P-spray	2×10^{13}	513	2.56	93.17
	1×10^{14}	495	2.44	89
Optimized Modulated P-spray	2×10^{13}	1600	1.58	93.22
	1×10^{14}	1150	1.60	89

210 technique.

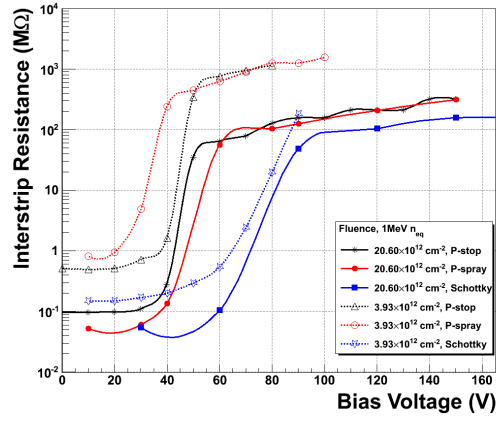


Figure 21: Comparison of R_{int} vs. V_{bias} for DSSDs equipped with P-stop, P-spray and Schottky barrier at low and high fluences.

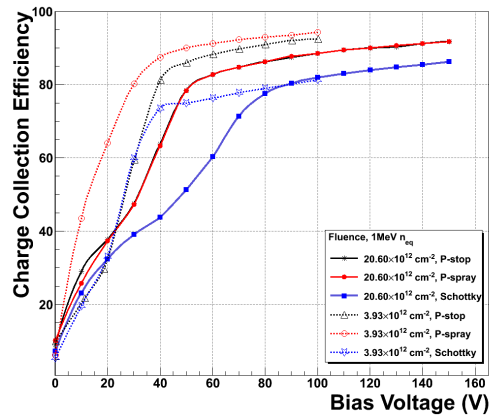


Figure 22: Comparison of CCE vs. V_{bias} for DSSDs equipped with P-stop, P-spray and Schottky barrier at low and high fluences.

211 An optimization study has been done for modulated P-spray in terms of P-spray dose and P-stop width for the
 212 maximum expected fluence of $1 \times 10^{14} \text{ n}_{eq} \text{ cm}^{-2}$. It is known that narrow P-stop improves the V_{bd} but deteriorates the

213 C_{int} [23, 24] while in the case of P-spray, higher dose implies premature breakdown and higher C_{int} for the p-type
 214 substrate. We have taken various combinations of P-stop width and P-spray dose and extracted the V_{bd} and C_{int} . As
 215 can be seen from Table 5, the C_{int} increases and V_{bd} decreases with P-spray dose for a fixed P-stop width. Also, one
 216 can observe from Table 5 that for a fixed P-spray dose, the V_{bd} initially increases with P-stop width till 15 μm but
 217 deteriorates afterwards. This effect is more prominent for very low and low P-spray dose. From this table, it becomes
 218 clear that the best design criteria is to combine very low P-spray dose ($1 \times 10^{15} \text{ cm}^{-3}$) with 15 μm P-stop width, referred
 219 to as Optimized Modulated P-spray in Table 6. Finally a comparison of P-stop, P-spray and Optimized Modulated
 220 P-spray for 1st year of CBM run fluence ($2 \times 10^{13} \text{ n}_{eq} \text{ cm}^{-2}$) and the maximum fluence expected at the end of five years
 221 of CBM run ($1 \times 10^{14} \text{ n}_{eq} \text{ cm}^{-2}$) has been shown in Table 6. It is clear from this table that optimized modulated P-spray
 222 is the best choice for isolation technique in terms of V_{bd} , C_{int} and CCE.

223 4. Conclusions

224 This paper reports on the ongoing R&D effort to develop radiation hard low noise radiation hard DSSDs for
 225 the upcoming CBM experiment at FAIR. An optimization of isolation techniques has been done to maximize CCE
 226 and V_{bd} while minimizing the total ENC. Transient simulations has proven to be an effective tool to determine the
 227 operating voltage and to predict the expected CCE.

228 5. Acknowledgement

229 The authors would like to thank Dr.M.Merkin and Dr.D.Karmanov from SINP, Moscow State University, Rus-
 230 sia for irradiating CBM prototypes. We would also like to thank Dr.DavidPennicard from DESY, Germany and
 231 Dr.GemmaKerr from Microelectronics support centre, Rutherford Appleton Laboratory, UK for useful discussions
 232 and suggestions.

233 References

- 234 [1] <http://www.fair-center.eu/en/fair-users/experiments/cbm.html>
 235 [2] A. S. Brogna et al., "N-XYTER, a CMOS read-out ASIC for high resolution time and amplitude measurements on high rate multi-channel
 236 counting mode neutron detectors," NIM A, vol. 568, 2006, pp. 301-308.
 237 [3] G.Barichello et. al., "Performance of long modules of Silicon Microstrip detectors," NIM A, vol. 413, 1998, pp. 17-30.
 238 [4] C. Bozzi, "Signal-to-Noise evaluations for the CMS Silicon Microstrip Detectors," CMS note 1997/026.
 239 [5] <http://pdg.lbl.gov/2010/reviews/rpp2010-rev-particle-detectors-accel.pdf>.
 240 [6] [1]R.Wunstorf, "Radiation hardness of silicon detectors:current status," IEEE Trans. Nucl. Sci., vol. 44, 1997, pp.806.
 241 [7] [1]S.Chatterji et. al., "Simulation study of irradiated Si sensors equipped with metal- overhang for applications in LHC environment," vol.51
 242 (2), 2004, pp.298-312.
 243 [8] http://www.pfk.ff.vu.lt/lectures/funkc_dariniai/diod/schottky.htm
 244 [9] http://ecourses.vtu.ac.in/nptel/courses/Webcourse-contents/IIT-Delhi/Semiconductor%20Devices/metal_semi/lec1.htm
 245 [10] <http://www.synopsys.com/home.aspx>
 246 [11] "RD 48 Status Report", CERN/LHC 2000-009, Dec.1999.
 247 [12] [1]M. Moll et. al., " Investigation on the improved radiation hardness of silicon detectors with high oxygen concentration," NIM A, vol.439,
 248 2000, pp.282-292.
 249 [13] H.W.Kraner, Z.Li and K.U. Posnecker, "Fast neutron damage in silicon detectors," NIM A, vol.225, 1984, pp.615.
 250 [14] J.G.Fossum, R.P. Mertens, D.S. Lee, and J.F. Nijs, "Carrier Recombination and Lifetime in Highly Doped Silicon,"Solid-State Electron.,
 251 vol.26 (6), 1983, pp.569-576.
 252 [15] V.Eremin et. al., "Effect of radiation induced deep level traps on Si detector performance," NIM A, vol.476 (3), 2002, pp.537-549.
 253 [16] RD48 3rd Status Report, CERN/LHCC 2000-009.
 254 [17] G.Lindstrom et.al., NIM A 426 (1999)1.
 255 [18] W.Shockley and W.T.Read, "Statistics of the Recombinations of Holes and Electrons," Phys.Rev., vol.87 (5), 1952, pp.835-842.
 256 [19] M.Petasecca, F.Moscatelli, D.Passeri, G.U. Pignatel, "Numerical Simulation of radiation Damage Effects in p-Type and n-Type FZ Silicon
 257 Detectors," IEEE Trans. Nucl. Sci. NS-53 (5), 2006, pp.2971.
 258 [20] N.Tamura et.al., "Radiation effects of double-sided silicon strip sensors," NIMA, vol. 342(1), 1994, pp. 131-136.
 259 [21] G.Casse et.al., "Charge Collection Efficiency Measurements for segmented Silicon Detectors Irradiated to $1 \times 10^{16} \text{ n cm}^{-2}$," IEEE Trans. Nucl.
 260 Sci., vol.55 (3), 2008, pp.1695.
 261 [22] T.Kawasaki, "The Belle Silicon Vertex Detectors," NIM A 494, 2002, pp.94-101.
 262 [23] C.Piemonte, "Device Simulations of Isolation Techniques for Silicon Microstrip Detectors Made on p-type Substrates," IEEE Trans. Nucl.
 263 Sci. vol.53 (3), 2006, pp.1694.
 264 [24] G.-F.Dalla Betta, "Surface Effects and Breakdown Voltage," MC-PAD Training Event, Ljubljana, 27 September, 2010.